Effective Area Tilt Impact In S+C+L Band Long-Haul Fiber Optic Transmission Systems

Viacheslav V. Ivanov(1), Petr M. Sterlingov(1), Snigdharaj K. Mishra(2) , John D. Downie(3), Sergejs Makovejs(4)

(1) Corning Scientific Center, Shatelena 26A, St. Petersburg, Russia, 194021
(2) Corning Research and Development Corporation, 310 N. College Rd, MS-6, Wilmington, NC 28405
(3) Corning Research and Development Corporation, SP-AR-02-1, Corning, NY 14870 USA
(4) Corning Optical Communications, Lakeside Business Village, CH5 3XD, UK,
Email: ivanovvv@corning.com

Abstract: In this paper we investigate the impact of effective area tilt on the performance of wideband fiber optic transmission systems, and quantify transmission performance variability associated with the use of different types of terrestrial fibers.

Introduction

Increasing cable capacity in long-haul transmission is of paramount importance nowadays. One of the ways to further increase optical cable capacity is to employ band division multiplexing [1], by adding channels in the S- and L- bands around 1450-1520 nm and 1575-1620 nm along with C-band transmission between 1530 and 1570 nm. C+L transmission has already been widely deployed [2], and S+C+L deployment for short- and mid-haul terrestrial applications is also being studied within research community. Previous modeling approaches utilized the ISRS-GN model [4] and subsequently its modifications including EGN generalization [5], and the impact of non-instantaneous nonlinear response [6].

In this work we review and combine a formalism to include effective area tilt in S+C+L band systems modeling. We propose an ISRS-GN model modification to capture FWM interaction in the fiber with varying nonlinear coefficient across frequency triplets. We also compare different fiber type performances in S+C+L in terms of total cable capacity and lowest channel capacity dependences vs distance. We observe degradation of S-band channels predicted capacity by up to 7% if effective area tilt is included. We find that larger effective area fibers (e.g. G.654.E-compliant fibers) offer enhanced performance and capacity in these systems. To the best of our knowledge, this is the first detailed investigation of the impact of effective area scaling on the transmission performance of ultra-wideband systems.

1. Model description

The impact of effective area (A_{eff}) tilt vs wavelength on system performance can be modeled with varying degree of accuracy. Raman gain coefficient (g_R) is often assumed to be simply inversely proportional to effective area [7]. However, as pointed out in [8], the dependence of g_R vs wavelength is not strictly inversely proportional to A_{eff}, but has a rather steeper dependence and may be more accurately described as follows:

$$\frac{g_R(f_p)}{g_R(f_{p,ref})} = \left(\frac{f_p}{f_{p,ref}}\right)^{1+0.1+n_A} \qquad \frac{A_{eff}(f)}{A_{eff,}(f_{ref})} = \left(\frac{f}{f_{ref}}\right)^{-n_A} \tag{1}$$

Here $f_{p,ref}$ is the reference pump frequency at which $g_R(f_{p,ref})$ is given, and f_p is the pump frequency at which $g_R(f_p)$ is evaluated. The A_{eff} scaling term n_A is defined as an effective area scaling exponent. The effective area of the fiber needs to be known at reference frequency f_{ref} to be scaled to arbitrary frequency f. According to [8], the 1+0.1 term in the exponent of the Raman gain coefficient g_R frequency dependence arises from the expression below:

$$g_R(f) \propto \frac{f[n^2(f)-1]}{n(f)n(f)\,A_{eff}} \tag{2}$$

where *n(f)* is the refractive index of silica glass. The first factor *f* leads to the "1" contribution and factors containing *n(f)* lead to the "0.1" contribution through the Sellmeier equation. As a result, this value may change depending on glass composition. This model assumes that it is sufficient to know the A_{eff} frequency dependence to estimate g_R frequency dependence, but this may not be true in general, as pointed out in [8]. This is because dependences of g_R vs. frequency shift and vs. pump frequency are not separable. However, as our modeling shows below, such subtleties have small impact on system performance, hence the given approximation is acceptable.

The fiber nonlinearity coefficient γ is given by:

$$\gamma = \frac{2\pi n_2 f}{A_{eff} \cdot c} \tag{3}$$

where n_2 is the nonlinear refractive index and c is the speed of light. In [9], γ is scaled linearly with respect to the mode field diameter of the fiber at various wavelengths. As pointed out in [10, Chapter 2], γ can be scaled according to the f term only, while n_2 and A_{eff} dependences can be neglected for bandwidths up to 20 THz. Although the bandwidth of an S+C+L system is within 20 THz, in this work we include f and A_{eff} scaling while keeping n_2 constant. n_2 frequency dependence can be included according to the methodology described in [11]. Thus, the final formula for γ tilt using Eqs. (1) and (3) can be given as:

$$\frac{\gamma(f)}{\gamma(f_{ref})} = 1 + \frac{f}{f_{ref}} - \left(\frac{f}{f_{ref}}\right)^{-n_A} \tag{4}$$

For nonlinear noise power evaluation, we used a closed-form ISRS-GN model [12], which includes modulation format correction terms and relies on SPM+XPM NLI power approximation. The delayed nonlinear response terms [6] were neglected. We added a parametric fitting to improve the accuracy of NLI power estimation at the spectrum edges [13]. The fitting procedure is implemented similarly to [14]. In this work the nonlinear noise power in the ISRS-GN model is scaled quadratically with respect to γ, according to ISRS-GN model formalism [4]:

$$G(f) = \frac{16}{27}\gamma^2 \int df_1 \int df_2\, G_{Tx}(f_1) G_{Tx}(f_2) G_{Tx}(f_1+f_2-f) \left| \int_0^L d\zeta \sqrt{\frac{\rho(\zeta,f_1)\rho(\zeta,f_2)\rho(\zeta,f_1+f_2-f)}{\rho(\zeta,f)}}\, e^{j\phi(f_1,f_2,f,\zeta)} \right|^2 \tag{5}$$

All quantities presented in Eq. 5 are further described in [4]. In the original GN model derivation from Manakov equation [15] given by Eq. 6, a linear field complex transfer function Γ(f,z), includes not only power evolution $g(z,f)$ and dispersion $j\beta(f)z$ factors, but also $\gamma(f)\cdot\sum_f P(z)$ term, given that nonlinear field is decomposed according to [15 Eq. 37].

$$\frac{\partial E_x}{\partial z} = \Gamma(z,f)E_x + \frac{8}{9}\gamma(f)E_x(E_x E_x^* + E_y E_y^*) \tag{6}$$

$$\Gamma(z,f) = -j\beta(f)z - \int_0^z d\zeta' \cdot \left[j\psi(\zeta',f) + \frac{g(\zeta',f)}{2} \right] \qquad \psi(z,f) = \sqrt{\frac{1}{2^3}\frac{8}{9}}\, \gamma(f)\cdot\sum_f P(z,f) \tag{7}$$

This differs from the ISRS-GN derivation [4], but results in equivalent formulas for GN and ISRS-GN models when ISRS power transfer and nonlinear coefficient frequency dependence are neglected. The factor $\sqrt{\frac{1}{2^3}\frac{8}{9}}$ arises from solving Eq. (6) according to GN model assumptions. We neglected the impact of $\psi(z,f)$ term, because we do not expect a significant impact of this term in S+C+L band systems. However, for generality and for wider bandwidth systems, the inclusion of FWM interactions between frequency components with different nonlinear coefficients can become important. The effect may be included by additional phase factor within integrals of ISRS-GN model, given by Eq. (8) along with dispersion factor:

$$e^{j\phi(f_1,f_2,f,\zeta)} = e^{j[\beta(f_1)-\beta(f_1+f_2-f)+\beta(f_2)-\beta(f)]\zeta} \cdot e^{j\int_0^\zeta d\zeta'[\psi(\zeta',f_1)-\psi(\zeta',f_1+f_2-f)+\psi(\zeta',f_2)-\psi(\zeta',f)]} \tag{8}$$

A closed-form version of the ISRS-GN model [12] must be rederived due to a distance dependence of this phase term, which has not been accounted for in prior research work. To calculate power evolution along the propagation distance $P(z,f)$, a system of coupled Raman differential equations for each channel i is used:

$$\frac{\partial P_i}{\partial z} = P_i \cdot \left(-\alpha_i + \sum_{j=0}^{i-1} P_j \cdot g_R^j - \sum_{k=i+1}^{N_{ch}-1} P_k \cdot g_R^k \cdot \frac{f_i}{f_k} \right) \tag{9}$$

Here, f_i/f_k represents a quantum loss of energy due to energy level transfer. To include Raman gain coefficient scaling described in Eq. 1 into Eq. 9, g_R^j and g_R^k are evaluated at frequency shifts Δf and pump frequences f_p as:

$$g_R^j = g_R[\Delta f = f_i - f_j;\ f_p = f_j] \qquad\qquad g_R^k = g_R[\Delta f = f_k - f_i;\ f_p = f_i] \tag{10}$$

For modeling results shown in the next section, we also employed a channel launch power optimization procedure similar to [13], to maximize overall fiber capacity, which consisted of a series of gradient-descent optimizations.

2. Results

In this work we used measured fiber spectral attenuation and $g_R(\Delta f)$ profiles for Corning® SMF-28® ULL, Corning® TXF® and Corning® SMF-28® Ultra fibers. A_{eff} spectral dependence was obtained through fundamental simulations with refractive index profiles. Other fiber parameters can be found in product specifications [16], with typical attenuation values at 1550 nm 0.158 dB/km for SMF-28 ULL fiber, 0.166 dB/km for TXF fiber, and 0.183 dB/km for SMF-28 Ultra fiber. Assumed A_{eff} values at 1550 nm were 83 μm^2, 125 μm^2 and 80 μm^2, and scaling factors n_A as captured from A_{eff} spectral dependence were 0.9, 1.46 and 1.4, respectively. The system links, amplifiers, and channel parameters modeled here are similar to [17], with 75 km spans and 50 GHz spaced channels at 32 Gbaud.. The total bandwidth was up to 20 THz, which included the gaps between 1520 and 1530 nm and 1565 and 1570 nm. Assumed modulation format kurtosis for ISRS-GN model is -0.6. EDFA noise figure profile is taken from equipment specifications [3] and power tilt due to ISRS is assumed to be ideally compensated by attenuators after each span, to avoid rapid transmission performance degradation in the presence of high-gain terrestrial amplifiers. Fig. 1 shows channel capacity modeling results with both ASE and NLI noises. Dotted lines correspond to the scenario in which effective area tilt is neglected, dashed line represents the case where only g_R tilt is included, and solid lines are for the case where both the g_R and γ tilt vs. wavelength are included. The g_R tilt impact remains small, with maximum capacity deviation of 2%, suggesting the validity of Raman gain coefficient scaling according to simple effective area inverse proportionality. γ tilt increases the performance variation over the bandwidth and leads to smaller capacities in S-band (up to 7%) and slightly greater capacities in the L-band (1%). The variation of channel capacities in the S-band is caused by variations of Thulium doped fiber amplifier noise figure from 6 to 8 dB, of fiber attenuation by 0.04 dB and of the optimized launch powers by 4 dB. In the Figs. 2-3 we included both g_R and γ wavelength variations and assessed the relative performance of different fiber types in terms of system capacity vs. distance and bandwidth. The best performance is obtained with the large effective area fiber (TXF fiber), which has the most rapid growth of total fiber capacity versus bandwidth and the highest capacity of the worst-case channel. While TXF fiber is G.654.E-compliant and may have cable cut-off wavelength of up to 1520 nm, we are currently pursuing a more detailed modeling of S-band performance under realistic fiber bend conditions in a terrestrial cable and splice trays. The results shown here are representative of what could be expected for this fiber with cable cutoff < 1450 nm or if multipath interference compensation is employed in the DSP of the coherent receiver, as previously demonstrated [18].

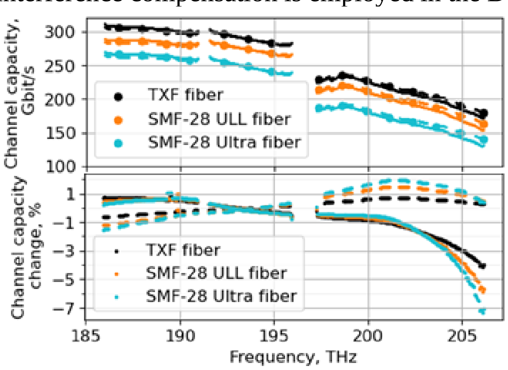

Fig. 1. Top. Channel capacity vs frequency at 7500 km distance and 20 THz. Solid line: g_R and γ Aeff dependencies included; dashed line: g_R only included; markers: no Aeff dependence. Bottom: deviation of solid and dashed line from markers

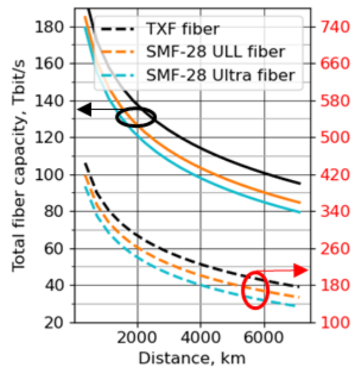

Fig. 2. Capacities vs distance for 20 THz bandwidth

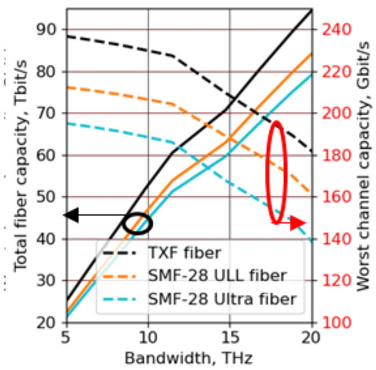

Fig. 3. Capacities vs bandwidth at 7500 km. Bandwidth is increased starting from C-band and by adding L-band channels and then S-band channels.

Conclusions

In this paper we outlined a model of ultra-wideband coherent optical transmission systems including the impact of fiber effective area tilt. We found that inclusion of A_{eff} tilt in the nonlinear coefficient leads to greater performance variation over the full bandwidth, degrading S-band performance by up to 7% and improving L-band performance by 1%. We presented the nonlinear noise model modification which accounts for FWM interactions between frequency-triplets with varying nonlinear coefficient, and concluded such a model may be important for ultra-wideband modeling. We also compared the performance of different terrestrial fibers in S+C+L wideband systems in the presence of global launch power optimization and observed benefits up to 15% in total capacity and up to 40% in worst-case channel capacity from lower attenuation and larger effective area fibers in wideband applications.

References

[1] A. Ferrari *et al*, in *JLT*, vol. 38, no. 5, pp. 1041-1049, 1 March1, 2020, doi: 10.1109/JLT.2020.2970484.
[2] M. Cantono *et al*, in *JLT*, vol. 38, no. 5, pp. 1050-1060, 1 March1, 2020, doi: 10.1109/JLT.2019.2959272.
[3] Fiberlabs Inc. AMP-FL8221-SB-16 amplifier datasheet.
[4] D. Semrau *et al*, in *JLT*, vol. 36, no. 14, pp. 3046-3055, 15 July15, 2018, doi: 10.1109/JLT.2018.2830973.
[5] H. Rabbani *et al*, arXiv, 2020, [1909.08714].
[6] D. Semrau *et al*, in *JLT*, vol. 39, no. 7, pp. 1937-1952, 1 April 1, 2021, doi: 10.1109/JLT.2020.3046998.
[7] I. Roberts *et al.*, in *JLT*, vol. 35, no. 23, pp. 5237-5249, 1 Dec.1, 2017, doi: 10.1109/JLT.2017.2771719.
[8] N. R. Newbury, in *JLT*, vol. 21, no. 12, pp. 3364-3373, Dec. 2003, doi: 10.1109/JLT.2003.821716
[9] G. Saavedra *at al*, *arXiv preprint arXiv:1910.03045* (2019).
[10] G. Agrawal, "Nonlinear Fiber Optics 6th edition", Academic Press, Aug. 2019, pp 37-39.
[11] A. Ahmed *et al*, *2012 7th International Conference on Electrical and Computer Engineering*, 2012, pp. 389-392, doi: 10.1109/ICECE.2012.6471569.
[12] D. Semrau *et al*, *45th European Conference on Optical Communication (ECOC 2019)*, 2019, pp. 1-4, doi: 10.1049/cp.2019.0892.
[13] D. Semrau *et al* in *JLT*, vol. 37, no. 9, pp. 1924-1936, 1 May1, 2019, doi: 10.1109/JLT.2019.2895237.
[14] M. R. Zefreh *et al*, *arXiv preprint arXiv:2006.03088* (2020).
[15] Poggiolini, Pierluigi, *et al.*, *arXiv preprint arXiv:1209.0394* (2012).
[16] Optical Fiber datasheets Corning® SMF-28® ULL, Corning® SMF-28® Ultra and Corning® TXF® available online.
[17] B. Correia *et al.*, *J. Opt. Commun. Netw.* 13, 147-157 (2021).
[18] J. D. Downie *et al.*, in *IEEE Journal of Selected Topics in Quantum Electronics*, vol. 23, no. 3, pp. 31-42, May-June 2017, Art no. 4400312, doi: 10.1109/JSTQE.2016.2617208.